

COSMIC RAY MEASUREMENTS WITH IceCube*

HERMANN KOLANOSKI

for the IceCube Collaboration

Humboldt Universität zu Berlin, Germany

and

DESY, Zeuthen, Germany

*Received 12 April 2022, accepted 13 May 2022,**published online 9 September 2022*

We report on measurements of cosmic rays in the energy range between some 100 TeV and about 1 EeV using the IceCube Neutrino Observatory at the South Pole. The IceCube facility combines the in-ice detector with the 1-km² surface detector IceTop. The combination offers a unique possibility to study the air-shower development at the surface together with the high-energy muons and neutrinos generated in the first interactions in the upper atmosphere. The report gives an overview of experimental results and a discussion of their impact on the understanding of cosmic rays and of hadronic air-shower models. Finally, we briefly discuss the ongoing upgrade activities for the current surface detector and for the future extensions (IceCube-Gen2).

DOI:10.5506/APhysPolBSupp.15.3-A1

1. Introduction

The IceCube Neutrino Observatory (Fig. 1) is a 1-km³ detector situated in the ice of the geographic South Pole at a depth of about 2000 m [1]. IceTop, the surface component of IceCube, is an air-shower array covering the energy range from about 10¹⁴ eV to 10¹⁸ eV [2] that is the energy range between direct measurements with balloons and satellites and the highest energies tackled by experiments such as TA and Auger. Besides serving for the physics of charged cosmic rays, the surface array is also employed as a veto against cosmic-ray induced background in the search for astrophysical neutrinos with IceCube.

* Presented at the 28th Cracow Epiphany Conference on *Recent Advances in Astroparticle Physics*, Cracow, Poland, 10–14 January, 2022.

Cosmic-ray physics is performed with the air-shower array IceTop as well as with the in-ice detector IceCube, both independently or together in coincidence. While IceTop exploits the air showers, the in-ice detector provides the detection of high-energy muons or muon bundles. The coincidence measurements are the particular strength of IceCube, supplying a powerful handle for the determination of the mass composition.

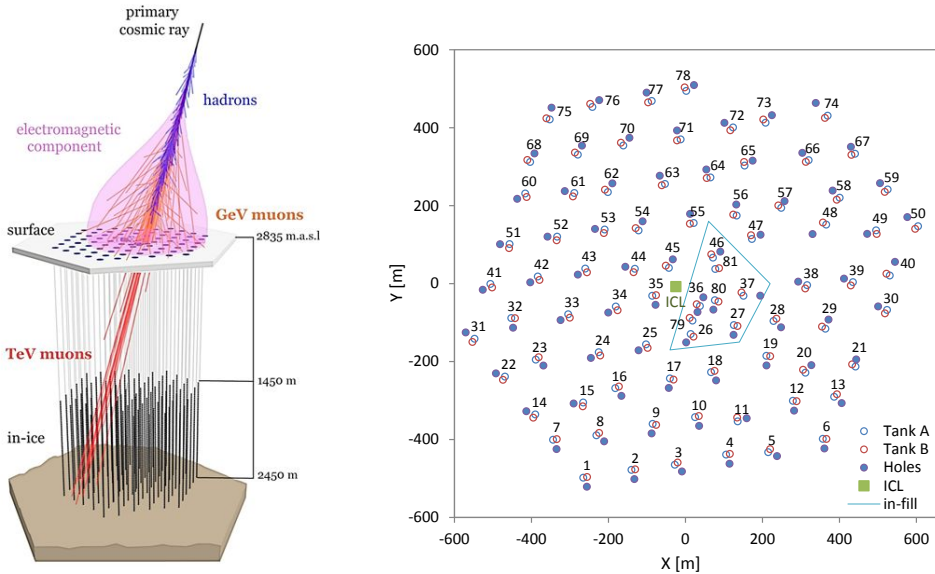


Fig. 1. (Color online) The IceCube Observatory. Shown are the in-ice detector and the surface array IceTop.

2. The detector

IceCube: IceCube's main component is an array of 86 strings equipped with 5160 light detectors in a volume of 1 km^3 at a depth between 1450 m and 2450 m [1]. In the lower part of the detector, a section called DeepCore is more densely instrumented. The main purpose of IceCube is the detection of high-energy neutrinos from astrophysical sources via the Cherenkov light of charged particles generated in neutrino interactions in the ice or the rock below the ice. In the context of cosmic-ray physics, it allows for the detection of high-energy muons and neutrinos generated in air showers initiated by cosmic rays.

IceTop: The IceTop air-shower array [2] is located above IceCube at a height of 2832 m above sea level, corresponding to an atmospheric depth of about 690 g/cm^2 . It consists of 162 ice Cherenkov tanks, placed at 81 stations and distributed over an area of 1 km^2 on a grid with mean spacing of 125 m. In the center of the array, three stations have been installed at

intermediate positions. Together with the neighboring stations, they form an in-fill array for denser shower sampling allowing for lower energy thresholds. Each station comprises two cylindrical tanks, 10 m apart from each other, with a diameter of 1.86 m and filled with 90 cm of ice. The tanks are embedded into the snow so that ideally their top surface is level with the surrounding snow to minimize temperature variations and snow accumulation caused by wind drift. However, snow accumulation (mainly due to irregular snow surfaces) cannot be avoided so the snow height has to be monitored and taken into account in simulation and reconstruction (this is a source of non-negligible systematic uncertainties).

Each tank is equipped with two ‘Digital Optical Modules’ (DOMs), each containing a 10" photo multiplier tube (PMT) to record the Cherenkov light of charged particles that penetrate the tank. In addition, a DOM houses complex electronic circuitry supplying signal digitization, readout, triggering, calibration, data transfer, and various control functions. DOMs, electronics, and readout scheme are the same as for the in-ice detector [1].

To initiate the readout of DOMs, a local coincidence between the tanks of a station is required. Additionally, IceTop is always read out in the case of a trigger issued by another detector component (and *vice versa*). For each single tank above the trigger threshold, even without a local coincidence, condensed data containing integrated charge and time stamp are transmitted. These so-called SLC hits (SLC = ‘soft local coincidence’) are useful for detecting single muons in shower regions where the electromagnetic component has mostly or fully been absorbed (low energies, outer region of showers, inclined showers). For IceTop, the measured charges are expressed in units of ‘vertical equivalent muons’ (VEM) determined by calibrating each DOM with muons.

3. All-particle spectrum (IceTop only)

The determination of the spectrum and mass composition of the charged cosmic rays is a key topic of IceCube’s cosmic-ray program. The IceCube Collaboration published several analyses of the spectrum which are different in methods and/or in the covered energy range. Analyses done with IceTop only, without the information of the high-energy muons detected in the deep detector, allow for a wider zenith-angle range since a coincidence is only possible for zenith angles smaller than about 30° . The signals recorded by the surface tanks yield the energy deposited by the shower particles together with the arrival times. This information is used to reconstruct the shower energy and direction by fitting the lateral shower distribution around the shower axis. The shower axis is mainly determined by the arrival times of the signals. The lateral distribution of the tank signals, $S(R)$, at a distance R

from the shower axis is fitted by the Lateral Distribution Function (LDF)

$$S(R) = S_{125} \left(\frac{R}{125 \text{ m}} \right)^{-\beta - 0.303 \log_{10} \left(\frac{R}{125 \text{ m}} \right)} f_{\text{snow}}, \quad (1)$$

which is equivalent to describing the logarithm of the tank signals as a second-order polynomial in the logarithm of R . The shower size is characterized by the signal S_{125} at a reference radius of 125 m. Furthermore, we refer to β , the slope of the logarithm of the LDF. The function f_{snow} accounts for the signal attenuation due to snow coverage.

The shower size parameter S_{125} is used as an energy proxy. Although it is chosen to minimize dependencies on other parameters, like the mass of the primary, the relation between S_{125} and the energy of the primary cosmic ray has a slight mass dependence. Since in the IceTop-only approach, one does not directly determine the mass, one has to use a model for the mass composition. We mostly refer to the H4a model [3]. Consistency of the model with the data can be checked by requiring that the same spectrum is obtained in all zenith angle directions since the shower development and absorption depend on the slant depth in the atmosphere and are different for different masses of the primaries.

IceCube’s latest results on the all-particle spectrum using IceTop data only are shown in Fig. 2. The plot combines two IceTop analyses, one for energies from 2.5 PeV to 1.26 EeV [4] (only shown up to 200 PeV in the figure) and the other for energies from 250 TeV to 10 PeV [5]. The latter analysis

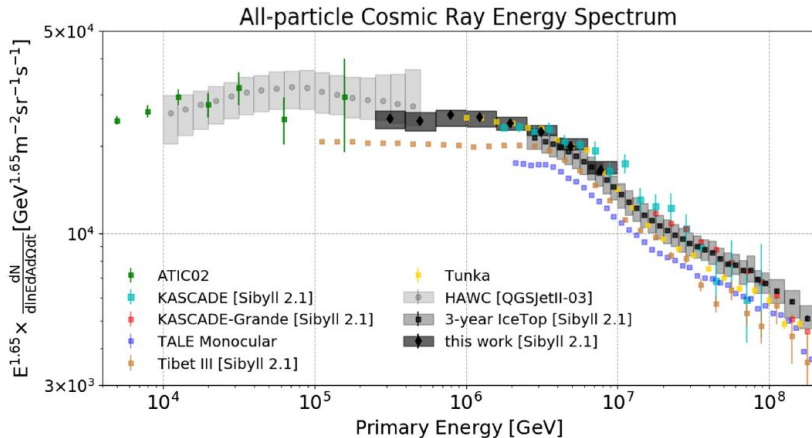


Fig. 2. (Color online) Cosmic-ray flux (differential in $\ln E$) using IceTop data scaled by $E^{1.65}$ and compared with fluxes from other experiments (references in [5]). Note that different hadronic interaction models are used by the experiments as indicated by the labels in the square-brackets.

exploits, for the first time, IceTop infill stations extending IceTop measurements to lower energies. In this way, the all-particle spectrum of IceTop connects at low energies to direct measurements and data from HAWC, a surface detector at a very high altitude [6]. The uncertainties are mostly dominated by systematics.

The two IceTop analyses, which use quite different trigger conditions and reconstruction methods, agree within their systematic uncertainties in the overlap region. At low energies, they connect well with the HAWC data and the direct measurements by the balloon experiment ATIC02 (see [5] for references). All spectra that cover the PeV region clearly confirm the knee feature around 4 PeV. In an earlier publication using less data [7], IceCube found that between the knee and 1 EeV, the spectrum exhibits a clear deviation from a single power law. The spectral index changes from $\gamma \approx -2.63$ below the knee to about $\gamma \approx -3.1$ above the knee, hardens around 18 PeV towards $\gamma \approx -2.9$ and steepens again around 130 PeV reaching $\gamma \approx -3.4$ [7].

4. Spectrum and composition: the role of muons

4.1. Mass-sensitive observables in air showers

In the high energy regime where cosmic rays cannot be directly measured, the mass composition of the primaries can only be inferred from the shower development in the atmosphere. All methods of mass determination are based on the model where a nucleus of mass number A and energy E shares its energy about equally between the A nucleons, hence the energy of nucleon i ($i = 1, \dots, A$) is

$$E_i = E/A. \quad (2)$$

At high energies, the nucleons can be assumed to interact independently, so that one has A independent shower developments. This yields various shower parameters to become dependent on the mass of the primary. For example, a shower composed of many showers at lower energies reaches the earlier the shower maximum, the more sub-showers contribute or, since the meson production and decay are energy-dependent, the muon multiplicity in an event becomes mass-dependent. While for the UHECR experiments the strongest handle for the determination of the mass composition is the measurement of the shower maximum, at lower energies the muon multiplicity is the preferred observable. Muons are mostly measured by the surface detectors. However, IceCube has the additional opportunity to measure high-energy muons in the TeV range (stemming from the first interactions in the atmosphere) and correlate their number per event with the (mainly electromagnetic) shower energy deposited in the surface detectors.

The energy dependence of the muon multiplicity can be approximated by a power law with an index $\beta \approx 0.9$ [8] such that the muon number per event becomes

$$N_\mu \propto A (E/A)^\beta = A^{1-\beta} E^\beta. \quad (3)$$

IceCube can measure multiplicities of TeV-muons in the deep ice as well as of GeV-muons with the surface detectors and can compare these muon counts to the electromagnetic shower component of an event as determined by the surface detector. In the case of GeV-muons, this comparison has only been done statistically averaging over many events. From the correlations, the mass composition can be deduced as will be shown in the following.

4.2. Cosmic-ray mass composition from TeV-muons

As already emphasized, a strength of IceCube is the possibility to measure high-energy muons in the deep ice in coincidence with the shower reconstructed in IceTop, as indicated in Fig. 1 (left). The muon bundle shown in the figure is narrower than the distance between the strings carrying the optical modules and thus individual muons cannot be resolved. Therefore, instead of the muon count, one exploits the energy deposited by the bundle and the spatial fluctuations of the deposition to get a handle on the muon number. High-energy muons (above the critical energy around 1 TeV) show strong deposition fluctuations along their trajectory due to bremsstrahlung. While the ionization energy loss occurs relatively smoothly and nearly energy independently, the energy deposition due to bremsstrahlung occurs more stochastically and is linearly increasing with energy. The surface detectors provide a calorimetric measurement of mainly the electromagnetic component of a shower, depending on the energy, mass, and zenith angle of the primary particle.

In the latest analysis of the spectrum and mass composition of cosmic rays [4], IceCube uses a neural network in order to exploit as many mass-dependent correlations as possible. As an example, the correlation between the energy deposited in the surface detectors and the energy deposited by the muon bundle in the deep ice is shown in Fig. 3 (left). The neural net has 5 inputs, two from the surface measurements (energy proxy S_{125} and zenith angle) and 3 from the in-ice measurements (an energy proxy and two ‘stochasticity’ variables). The net is trained to deliver the energy and mass of the primary. The training sample uses simulations of hydrogen, helium, oxygen, and iron.

While the net output for the energy reproduces the true energy quite well, the mass output for a given element is much more smeared, just because the correlation of the input variables with the mass is less strong than with the energy. Therefore, for each element and for each energy bin, the distributions

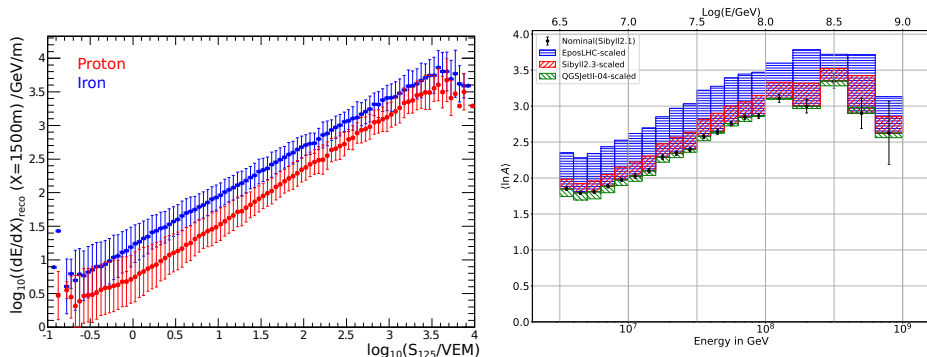


Fig. 3. (Color online) Left: Reconstructed energy loss as a function of S_{125} for proton (red/gray) and iron (blue/black) simulations, with the standard deviation indicated as error bars. Right: Determination of the average logarithmic mass of the primaries using, as a baseline for the training of the network, the hadronic interaction model Sibyll 2.1. The bands indicate the shift of the data points if another model is employed.

of the mass output are generated from simulations and used as templates for that element. In each bin, the four mass templates are fitted to the network output for the data yielding the relative contributions for each element at the considered energy. It is checked that the procedure interpolates well for the elements that the net is not trained for, so that each element contribution can stand for a group of neighboring elements.

The analysis yields the energy spectra for the four element groups. The sum of these spectra is the all-particle spectrum which is then independent of composition models. It agrees well with the IceTop-alone spectrum confirming the model used in this case. From the elemental energy spectra, one can also determine the average mass, conventionally one quotes the average logarithm of the mass, $\langle \ln A \rangle$, as a function of energy. Figure 3 (right) shows the results for $\langle \ln A \rangle$ obtained with the combined IceCube–IceTop analysis. The various sources of systematic uncertainties are discussed in paper [4]. Here, the plot depicts the dominating uncertainty due to the hadronic interaction model used for the network training. This uncertainty affects both the shower reconstruction as well as the predicted muon multiplicities per event. We will come back to the discussion of the dependencies on the hadronic interaction models in Section 4.4.

4.3. GeV-muons

With IceTop, the dominantly low-energy muons at the surface (‘GeV-muons’) can be analyzed. Although the surface array has no specific muon

detectors, muons can be identified by their energy deposits in the tanks yielding the characteristic peak of minimum-ionizing particles. With increasing distance from the shower axis, this muon peak becomes increasingly prominent in the tank's signal distribution. An example is shown in Fig. 4 (left) for a lateral distance of around 650 m and a primary energy around 10 PeV. The right panel of this figure shows the derived muon densities as a function of primary energy for distances of 600 m and of 800 m. The data are compared to the muon densities obtained from three different hadronic models for proton and iron. The plot shows that the models yield different primary compositions. This will be further discussed in the following section.

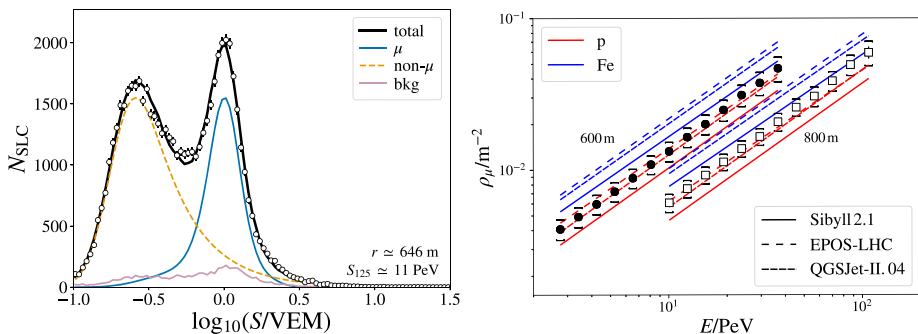


Fig. 4. (Color online) Left: Signal distribution of tanks at mean lateral distances of 646 m from the shower axis. The distribution is fitted by a model containing the muon contribution and backgrounds. The given S_{125} value corresponds to primary energies near 10 PeV. Right: Measured muon density at 600 m (solid circles) and 800 m (white squares) lateral distance after applying corrections averaged over the different models used for the simulations. Error bars indicate the statistical uncertainty, brackets the systematic uncertainty. Shown for comparison are the corresponding simulated densities for proton and iron (red and blue lines, respectively).

4.4. Tests of hadronic interaction models

For the interpretation of air shower measurements, a correct modeling of the hadronic interactions of shower particles in the atmosphere is crucial. There are various models by different authors which, however, in general yield different results for the same measurement. Therefore, it is important to test the validity of the models and obtain hints for improvements. There are new model versions on the market which have been updated using LHC data. Therefore, one distinguishes between ‘pre-LHC’ and ‘post-LHC’ models.

With IceCube, hadronic interactions of air showers can uniquely be tested by simultaneously measuring the electromagnetic component and both the GeV-muon and TeV-muon components of air showers. The hadronic

interaction models Sibyll 2.1, QGSJet-II.04, and EPOS-LHC (the latter two are post-LHC models) have been tested by comparing data to simulations of proton and iron showers [9]. As a measure of the mass composition, one defines a variable z quantifying the composition in the range between proton and iron

$$z = \frac{x_{\text{data}} - x_p}{x_{\text{Fe}} - x_p}, \quad (4)$$

where x is one of the mass-sensitive observables obtained from data. The quantities x_p and x_{Fe} are derived from proton and iron simulations, respectively, employing one of the hadronic models. The tested mass-sensitive observables are the fitted slope β of the lateral shower distribution, a proxy for the energy deposition of the muon bundle in the deep detector, $\ln(dE/dX_{1500})$, and the GeV-muon densities at two distances, $\ln(\rho_{\mu,600})$ and $\ln(\rho_{\mu,800})$.

Figure 5 shows, for two of the models, the z distributions of the composition-sensitive observables as a function of the primary energy estimator S_{125} . If the models give a realistic description of experimental data, all z distributions should be the same within errors.

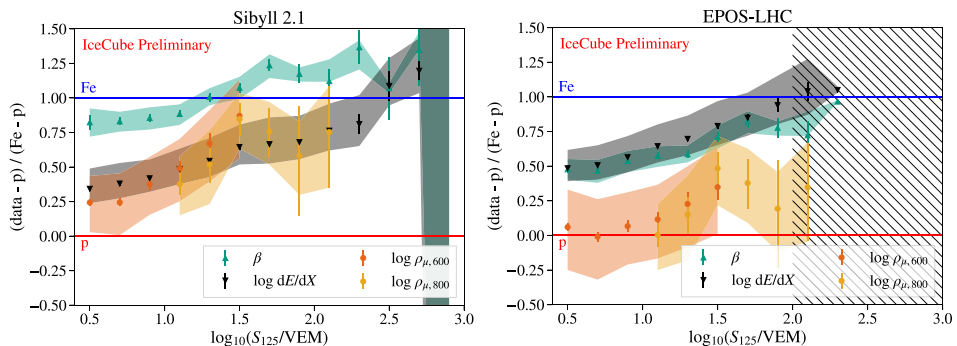


Fig. 5. (Color online) Distribution of the different composition-sensitive observables as a function of the primary energy estimator S_{125} in proton–iron space as represented by the z values. The error bars show the statistical uncertainty, while the bands represent the systematic uncertainties. Due to limited availability of simulations, the results for EPOS-LHC are limited to $\log_{10} S_{125}/\text{VEM} = 2$. From [9].

However, one observes internal inconsistencies within one model and disagreements between the two shown models. In both models, the slope of the lateral shower distribution does not agree with the distribution of the low-energy muons. Within the model Sibyll 2.1, the slope even takes non-physical values beyond the line for iron, while the distributions for high- and low-energy muons agree reasonably.

In air showers initiated by cosmic rays above about 1 EeV, the measured densities of low-energy muons (around 1 GeV) are always higher than the predictions from simulations, even taking non-physical values above the predictions for iron. This problem could not be solved by tuning the models with LHC data. In our data, at least up to 100 PeV, we do not find any indication that the muon densities could be too high. Instead, at the lowest primary energies, the post-LHC models tend to predict rather low muon densities (but still in the physical regime). As discussed in [10], it appears that the disagreement between ‘realistic’ predictions and observed muon densities increases with increasing energy.

These inconsistencies currently render it impossible to unambiguously determine the mass composition of cosmic rays by employing muon multiplicities. Therefore, it is of prime importance to investigate the causes for the inconsistencies and to make the models more realistic.

5. Seasonal variations of atmospheric muon and neutrino rates

Muon rates: The rate of high-energy muons in the deep ice, which are produced in the first interactions of cosmic rays with energies in the TeV range and above, exhibits seasonal variations which are correlated with the temperature in the higher atmosphere where the first interactions occur (data from May 2015 to December 2017 are shown in Fig. 6). Temperature variations cause variations in the density which then change the interaction probability of particles with the atmosphere. The interactions are in competition with decays — less interaction results in more decays with muons and neutrinos as decay products. The variation of the rate R is characterized by a correlation coefficient $\alpha_T(E_\mu)$ which is employed to describe the rate change as a

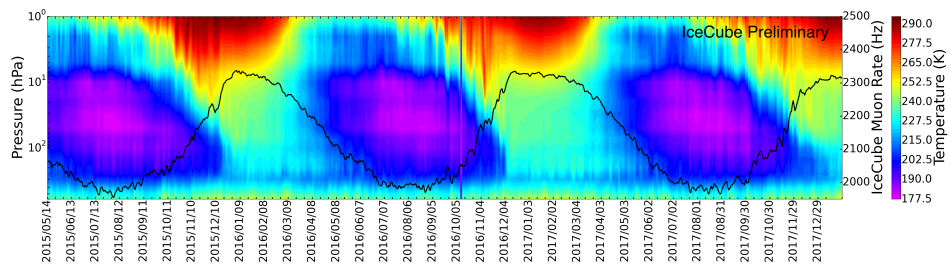


Fig. 6. (Color online) IceCube muon rate (black line) overlaid with the temperature profile of the South Pole atmosphere at different pressure heights. The plot illustrates the behavior of the seasonal cycles as well as the short-term (day to week time scales) variations in rate with respect to the temperature variations in the stratosphere.

linear function of the change of the so-called effective temperature

$$\delta R / \langle R \rangle = \alpha_T \times \delta T_{\text{eff}} / \langle T_{\text{eff}} \rangle. \quad (5)$$

The effective temperature $T_{\text{eff}}(\theta)$ is defined by the measured temperature profile (at a zenith angle θ) folded with the muon production spectrum and effective area for muon detection, and integrated over the muon energy spectrum

$$T_{\text{eff}}(\theta) = \frac{\int dE_\mu \int dX P_\mu(E_\mu, \theta, X) A_{\text{eff}}(E_\mu, \theta) T(X)}{\int dE_\mu \int dX P_\mu(E_\mu, \theta, X) A_{\text{eff}}(E_\mu, \theta)}, \quad (6)$$

with: X atmospheric slant depth, P_μ muon production yield, T atmospheric temperature profile, A_{eff} effective area for muon detection.

Since muons mainly come from decays of pions and kaons, which have different lifetimes and interaction probabilities, the coefficient $\alpha_T(E_\mu)$ is sensitive to the relative contributions of pions and kaons. Therefore, the measurement of $\alpha_T(E_\mu)$ yields another input for tuning hadronic models. The comparison of muon rate data for a specific year with the corresponding calculations in Fig. 7 demonstrates how well the temperature dependence of muon rates is understood (more details in [11]). Features, even small ones, are well reproduced by analytical calculations. However, data show a somewhat higher ΔR amplitude yielding $\alpha_T^{\text{meas}} = 0.75 < \alpha_T^{\text{calc}} = 0.85$. Calculations can still be refined (see also [12]), *e.g.*, by using a temperature profile instead of averages and by accounting for the muon multiplicity in the bundle and the mass composition.

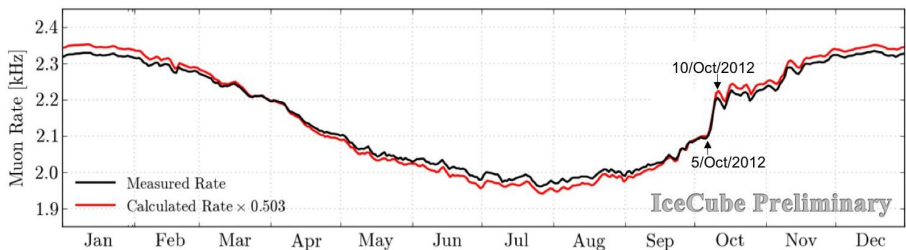


Fig. 7. (Color online) Comparison of the measured with the calculated muon rate for 2012 data.

Neutrino rates: A similar study has been done for seasonal variations of atmospheric neutrino rates [13]. While the muon data are obtained for the southern hemisphere, the neutrino data contain complementary information from the northern hemisphere, though with lower statistical significance. It adds to the complementarity that a neutrino has another kinematic relation with its parent particle (pion or kaon).

6. IceCube cosmic-ray anisotropy

6.1. Energy dependence of the cosmic-ray anisotropy

IceCube has studied the cosmic-ray anisotropy in a wide energy range between 10 TeV and 5 PeV [14, 15]. The arrival directions have been derived from muons in the deep ice, except for some measurements in the PeV range, where the direction has been obtained from showers in IceTop. While the shower measurements directly yield an estimate of the primary energy, for muons, the primary energy has been estimated from the energy deposited in the ice.

The main features of the observed anisotropy are:

- a dominant dipole at a relative intensity level of 10^{-3} ,
- a significant small scale structure at a level of 10^{-4} ,
- a phase shift of the dipole around 150 TeV,
- a turning point of the dipole amplitude at about 10 TeV.

If the anisotropies are due to magnetic fields, the latter observation could indicate a transition from the heliosphere to the interstellar magnetic field. The energy dependencies of the dipole phase and amplitude are depicted in Fig. 8.

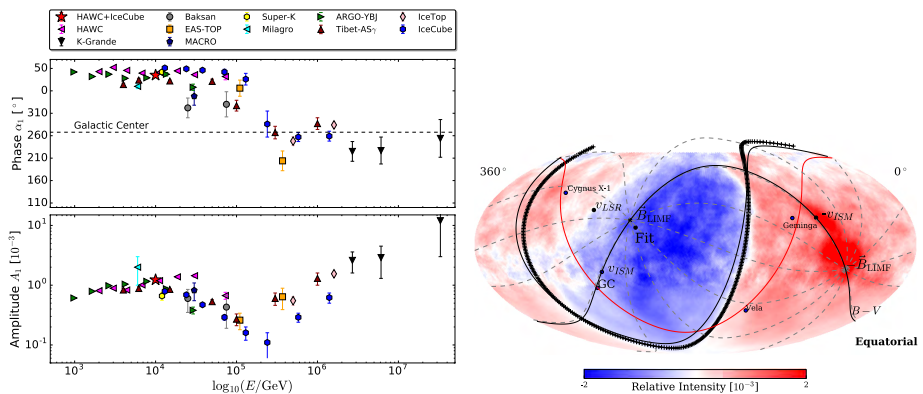


Fig. 8. (Color online) Left: Reconstructed dipole amplitude and phase from published TeV–PeV results from various experiments (adopted from [16]). Right: Relative intensity of cosmic rays at 10 TeV median energy in J2000 equatorial coordinates. The fit to the boundary between large-scale excess and deficit regions is shown as black crosses. The black curves are the magnetic equator from [17] and the plane containing the local interstellar medium magnetic field and velocity (B – V plane). The galactic plane is shown as a red curve. Indicated are also the Sun directions in the local rest frame (LSR) and in the interstellar medium (ISM).

Details of effects of magnetic fields require anisotropy analyses over the full sky. This cannot be achieved by a single experiment due to the restricted field of view (for example, IceCube sees the declination band from -16° to -90°). In the next section, we report on a combined analysis of the experiments HAWC and IceCube.

6.2. IceCube/HAWC all-sky anisotropy at 10 TeV

A full-sky analysis of the cosmic-ray arrival direction distribution has been performed with data collected by the HAWC and IceCube Observatories in the northern and southern hemispheres, respectively, at the same median primary particle energy of 10 TeV [18].

The combined sky map of the relative intensity of cosmic rays, that is the deviation from the intensity average in a declination band, is shown in Fig. 9. While the left plot shows clearly the dominance of a dipole, the right plot shows the small-scale structures remaining after subtraction of the leading multipoles with $\ell \leq 3$ in order to reveal structures smaller than 60° . The multipoles are determined by fitting spherical harmonics $Y_{\ell m}(\delta, \phi)$ to the sky map (δ , ϕ are declination and right ascension in equatorial coordinates). In this fit the $m = 0$ components, describing north–south effects, cannot be determined because the relative intensities are taken with respect to the average in a declination band.

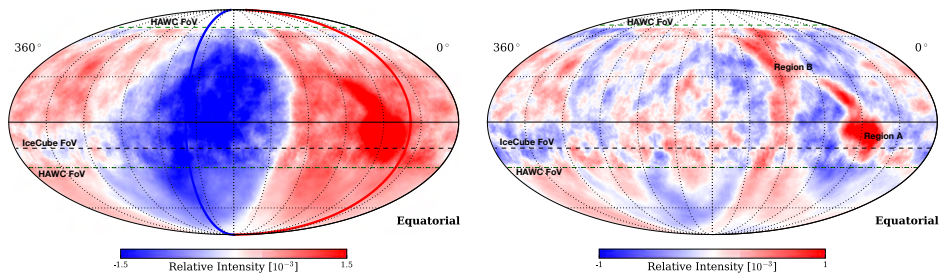


Fig. 9. (Color online) Left: Relative intensity of cosmic rays at 10 TeV median energy of the deviation from the average intensity in J2000 equatorial coordinates. The thick red and blue lines in the figure indicate, correspondingly, the node and antinode of the phase in R.A. of the dipole component from the fit. Right: Relative intensity after subtraction of the fitted leading multipoles. From [18].

6.3. Local interstellar magnetic field and heliosphere

The combined HAWC–IceCube analysis largely eliminates biases that result from partial sky coverage. The full sky coverage allows us to probe into the propagation of TeV cosmic rays through our local interstellar medium and the interaction between the interstellar and heliospheric magnetic fields.

Scattering on magnetic turbulences is a diffusive process and would, on large scales, lead to isotropy. Therefore, anisotropies are expected to originate from local effects (local sources, locally aligned fields, *etc.*) or movements, like the Compton–Getting effect due to the movement of the Earth around the Sun.

Figure 8 (right) shows directional correlations between the anisotropy structures and features of the local interstellar magnetic field (LIMF). An estimate of the dipole direction is obtained by fitting a plane along the boundary between large-scale excess and deficit. The fitted dipole axis points roughly in the direction of the LIMF as determined by independent observations [17]. If one assumes the dipole to be aligned with the LIMF, one could estimate the missing north–south dipole component ($m = 0$). A more detailed discussion can be found in [18].

7. Measurements of the Moon and Sun shadows

Absorption of cosmic rays by the Moon and the Sun causes observable deficits (shadows) in the cosmic-ray flux from the corresponding directions. These deficits can be used to verify the direction reconstruction of the detector and, in the case of the Sun, one can study the influence of the solar magnetic field on the temporal variation.

For such studies, IceCube uses the high-energy muons detected in the deep ice. The most recent and most comprehensive study of the Moon and Sun shadows, published in [19], uses seven years of data at median energies of about 50 to 60 TeV (the estimate is model dependent). While the Moon shadow is, as expected, consistent with the geometrical lunar-disk model, a time dependence has been observed for the Sun shadow during the time period from late 2010 until early 2017. This period covers a major part of solar cycle 24 which began in December 2008 and ended in December 2019. The deficit variation from year to year is correlated to the average sunspot number in the respective time period as can clearly be seen in Fig. 10 (left). The depicted linear fit excludes a constant deficit with a significance of 6.4σ . In Fig. 10 (right), the measured relative deficit is compared to the expectations from models of the solar magnetic field (see details in [19]). While data and models show similar behavior, quantitatively there are tensions leaving room for improvements of the models and refinement of the experimental studies.

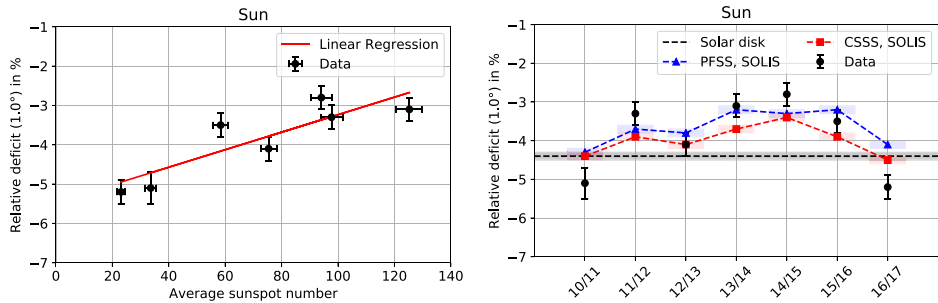


Fig. 10. (Color online) Left: Correlation of measured relative deficit due to the Sun shadow and average sunspot number. Right: Comparison of the measured relative deficit due to the Sun shadow to the deficit expected from different models of the solar magnetic field. The abscissa indicates the years of observation. The models are described and discussed in [19].

8. IceTop: hybrid detector enhancement

Currently, an enhancement program for IceTop is pursued. Detectors of various, complementary types are added to the existing array of IceTop tanks [20, 21]:

- scintillator panels,
- radio antennas,
- Cherenkov light telescopes (IceACT).

The plan of the layout of scintillator panels and radio antennas is shown in Fig. 11.

With this enhancement, the following improvements for cosmic-ray physics with IceCube should be achieved [22, 23]:

- reduction of systematic uncertainties due to snow coverage of the tanks (antennas and scintillators are elevated to avoid snow coverage),
- refinement of the cosmic-ray veto for neutrino searches,
- adding complementary measurements for composition determinations, like the shower maximum with radio measurements,
- opening the path towards a mass-dependence of the anisotropy,
- making searches for PeV gamma rays more competitive (until now only upper limits could be given),
- adding more input for tuning hadronic interaction models.

The surface enhancement also serves as a prototype for the surface array planned for the future extension IceCube-Gen2 [24].

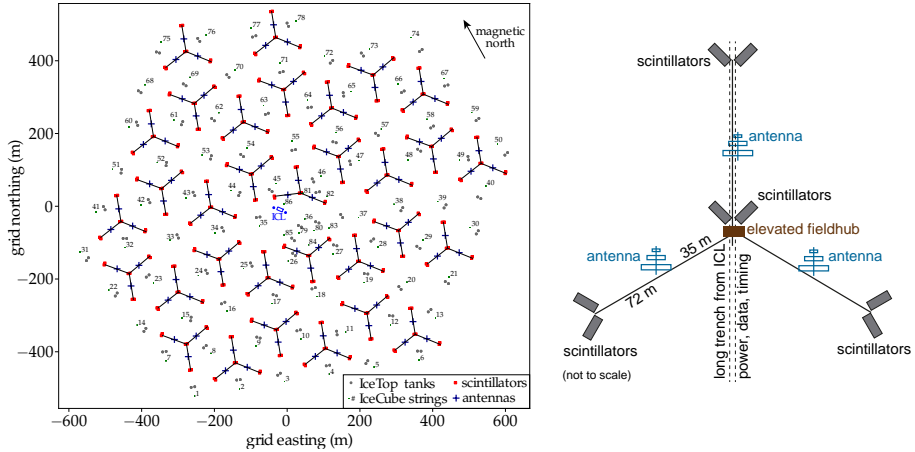


Fig. 11. (Color online) Layout of the scintillator-radio array (left) comprised of 32 stations (right).

REFERENCES

- [1] M.G. Aartsen *et al.*, «The IceCube Neutrino Observatory: instrumentation and online systems», *J. Instrum.* **12**, P03012 (2017).
- [2] IceCube Collaboration (R. Abbasi *et al.*), «IceTop: The surface component of IceCube», *Nucl. Instrum. Methods Phys. Res. A* **700**, 188 (2013).
- [3] T. Gaisser, «Spectrum of cosmic-ray nucleons, kaon production, and the atmospheric muon charge ratio», *Astropart. Phys.* **35**, 801 (2012).
- [4] IceCube Collaboration (M.G. Aartsen *et al.*), «Cosmic ray spectrum and composition from PeV to EeV using 3 years of data from IceTop and IceCube», *Phys. Rev. D* **100**, 082002 (2019).
- [5] IceCube Collaboration (M.G. Aartsen *et al.*), «Cosmic ray spectrum from 250 TeV to 10 PeV using IceTop», *Phys. Rev. D* **102**, 122001 (2020).
- [6] A. Tepe, «HAWC — The High Altitude Water Cherenkov Detector», *J. Phys.: Conf. Ser.* **375**, 052026 (2012).
- [7] IceCube Collaboration (M.G. Aartsen *et al.*), «Measurement of the cosmic ray energy spectrum with IceTop-73», *Phys. Rev. D* **88**, 042004 (2013).
- [8] K.-H. Kampert, M. Unger, «Measurements of the cosmic ray composition with air shower experiments», *Astropart. Phys.* **35**, 660 (2012).
- [9] IceCube Collaboration (S. Verpoest *et al.*), «Testing Hadronic Interaction Models with Cosmic Ray Measurements at the IceCube Neutrino Observatory», *PoS (ICRC2021)*, 357 (2021).
- [10] D. Soldin, «Update on the Combined Analysis of Muon Measurements from Nine Air Shower Experiments», *PoS (ICRC2021)*, 349 (2021).
- [11] IceCube Collaboration (S. Tilav *et al.*), «Seasonal Variation of Atmospheric Muons in IceCube», *PoS (ICRC2019)*, 894 (2020).

- [12] T. Gaisser, S. Verpoest, «Profiles of energetic muons in the atmosphere», *Astropart. Phys.* **133**, 102630 (2021).
- [13] IceCube Collaboration (P. Heix *et al.*), «Seasonal Variation of Atmospheric Neutrinos in IceCube», *PoS (ICRC2019)*, 465 (2020).
- [14] IceCube Collaboration (M.G. Aartsen *et al.*), «Anisotropy in Cosmic-ray Arrival Directions in the Southern Hemisphere Based on Six Years of Data from the IceCube Detector», *Astrophys. J.* **826**, 220 (2016).
- [15] IceCube Collaboration (M.G. Aartsen *et al.*), «Observation of Cosmic-ray Anisotropy with the IceTop Air Shower Array», *Astrophys. J.* **765**, 55 (2013).
- [16] M. Ahlers, P. Mertsch, «Origin of small-scale anisotropies in Galactic cosmic rays», *Prog. Part. Nucl. Phys.* **94**, 184 (2017).
- [17] E.J. Zirnstein *et al.*, «Local Interstellar Magnetic Field Determined from the Interstellar Boundary Explorer Ribbon», *Astrophys. J. Lett.* **818**, L18 (2016).
- [18] IceCube Collaboration (A.U. Abeysekara *et al.*), «All-sky Measurement of the Anisotropy of Cosmic Rays at 10 TeV and Mapping of the Local Interstellar Magnetic Field», *Astrophys. J.* **871**, 96 (2019).
- [19] IceCube Collaboration (M.G. Aartsen *et al.*), «Measurements of the time-dependent cosmic-ray Sun shadow with seven years of IceCube data: Comparison with the Solar cycle and magnetic field models», *Phys. Rev. D* **103**, 042005 (2021).
- [20] IceCube Collaboration (R. Abbasi *et al.*), «Development of a scintillation and radio hybrid detector array at the South Pole», *PoS (ICRC2021)*, 225 (2021).
- [21] IceCube Collaboration (R. Abbasi *et al.*), «Hybrid cosmic ray measurements using the IceAct telescopes in coincidence with the IceCube and IceTop detectors», *PoS (ICRC2021)*, 276 (2021).
- [22] IceCube Collaboration (F.G. Schröder), «Science Case of a Scintillator and Radio Surface Array at IceCube», *PoS (ICRC2019)*, 418 (2020).
- [23] IceCube Collaboration (A. Haungs *et al.*), «Cosmic-Ray Studies with the Surface Instrumentation of IceCube», *PoS (ICRC2021)*, 336 (2021).
- [24] IceCube-Gen2 Collaboration (F.G. Schroeder *et al.*), «The Surface Array planned for IceCube-Gen2», *PoS (ICRC2021)*, 407 (2021).